Structural, vibrational, and dielectric properties of Ruddlesden-Popper Ba_2ZrO_4 from first principles

Lydie Louis and Serge M. Nakhmanson*

Department of Materials Science & Engineering and Institute of Materials Science, University of Connecticut, Storrs, Connecticut 06269, USA

(Received 7 February 2015; revised manuscript received 24 March 2015; published 13 April 2015)

Using first-principles computational techniques, we have investigated the structural, vibrational, and dielectric properties of a Ruddlesden-Popper-type layered oxide Ba_2ZrO_4 subjected to a wide range of biaxial strains emulating epitaxial thin-film environment. Under compressive strains, this compound experiences an incommensurate distortion characterized by planar displacements of individual perovskite slabs away from their high symmetry positions. On the other hand, under increasing epitaxial tension, the original centrosymmetric structure becomes unstable—first, with respect to antiferrodistortive oxygen cage rotations and then also with respect to in-plane polar distortions. Both the incommensurate-to-commensurate and the nonpolar-to-polar phase transformations are accompanied by anomalies of the static dielectric response, however, only in the latter case a divergence of the in-plane dielectric constant is observed. Remarkably, even after the transition into the ferroelectric state (with polarization of up to 0.12 C/m^2 at 3.5% tension) dielectric permittivity of Ba_2ZrO_4 remains unusually high, which is explained by an emergence of a Goldstone-like excitation in the system manifested through an in-plane libration of the polarization vector. Since Ba_2ZrO_4 displays a yet poorly understood tendency to absorb small molecules, such as water and CO_2, acquiring better insights into the physical underpinnings of its behavior can produce more efficient functional materials for applications in advanced technologies for carbon sequestration.

DOI: 10.1103/PhysRevB.91.134103 PACS number(s): 77.84.−s, 77.80.bn, 63.22.Np

I. INTRODUCTION

ABO_3 perovskite oxides are well known for the wide range of useful dielectric, electrical and magnetic properties, encompassing ferroelectricity, ferromagnetism, ionic and electronic conduction, and superconductivity. In many instances, such properties are also functional, i.e., can be controlled by changes in chemical composition and microstructure, or tuned by applied electric, magnetic or elastic fields. Extensive theoretical and experimental investigations have been dedicated to mapping out the compositional space of perovskite oxides and establishing the associated structure-property-performance correlations. As a part of these efforts, the behavior of perovskite-oxide surfaces and, in particular, their interactions with a variety of different molecular species were evaluated for catalytic [1] and other advanced applications. For example, for a generic perovskite ferroelectric $PbTiO_3$, it was discovered that phase transitions and functional properties of its thin films could be influenced by controlling the nature and chemical potential of adsorbates deposited on their surface [2–4]. However, it was also recognized that, depending on the ambient and other environmental conditions, perovskite-oxide surfaces exhibit a dizzying array of complicated reconstructions [5–7] that are often challenging to quantify and control. The resulting stoichiometric changes greatly affect surface chemical properties, such as location of preferred adsorption sites, their energetics, atom exchange kinetics between the surface and the ambient, as well as any outcomes of surface-mediated chemical reactions.

Layered variations of the ABO_3 perovskite structures not only inherit the functional traits of their parents, but also possess a number of additional channels for property modification and fine-tuning. These materials are usually made up of quasi two-dimensional perovskite slabs stacked on top of each other, sometimes with other types of structural blocks sandwiched in between. Well-known homologous series of layered oxides based on slabs with (001) perovskite surfaces include Ruddlesden-Popper (RP; structural formula $A_{n+1}B_nO_{3n+1}$), Aurivillius, and Dion-Jacobson compounds [8,9]. Families based on other surface cuts, such as (110) and (111), have also been reported. Layered oxides properties can be modified by the choice of the cut and the chemical composition of the perovskite slab, which may in turn be single- or multicomponent (e.g., a superlattice), as well as by the adjustment of its thickness. Furthermore, although the individual slab surfaces in these materials are internal and no longer exposed to the ambient, their stoichiometry and functional characteristics can be manipulated via a wide variety of topochemical reactions. These reactions involve passage of ionic or molecular species through the interlayer spaces—also called interlayer galleries—as depicted in Fig. 1 for an "$n = 1$" A_2BO_4 RP compound [10,11]. Such remarkable flexibility of layered perovskites towards chemical manipulation (a trait that their ABO_3 counterparts do not possess in the same degree), combined with the wide variety of possible functionalities, makes these compounds especially attractive building blocks for the rational design of advanced materials for a variety of technological applications including, e.g., energy harvesting, storage, and conversion.

Layered-oxide compounds have been evaluated as catalysts in the photochemical splitting of water [12–17], which is currently the most promising technology to produce hydrogen fuel directly from such renewable sources like water and solar light [18]. They also show interesting behavior in the combined removal of particulate and NO_x, low-temperature oxidation of

*smn@ims.uconn.edu

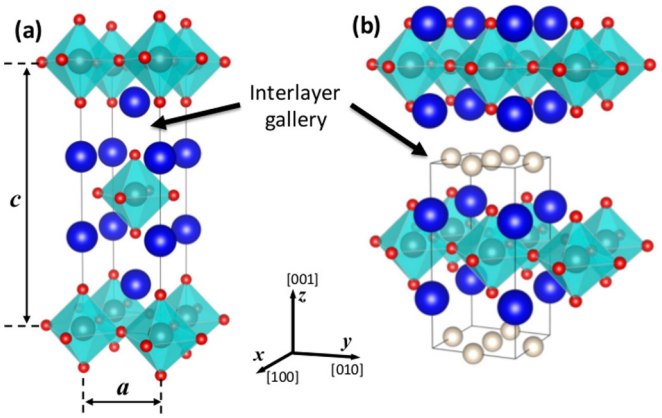

FIG. 1. (Color online) Schematics of the RP Ba_2ZrO_4 geometry. O and Ba atoms are shown as small red (medium gray) and large blue (black) spheres, respectively, while ZrO_6 cages are represented by semi-translucent octahedra. (a) Centrosymmetric $I4/mmm$ phase; lattice parameters a and c for the tetragonal unit cell used in the calculations are also shown. (b) Attachment sites for small molecules within the interlayer gallery are indicated by ivory spheres.

CO and methane oxidative coupling [19]. Specific advantages of utilization of these materials for photocatalysis stem from their highly-tunable electronic properties and the possibility to use their interlayer galleries for reaction sites, where electron-hole recombination processes could be retarded by physical separation of electron and hole pairs. A number of different layered perovskite-like oxides derived from $SrTiO_3$ and $LaTiO_3$ were probed in order to elucidate the structural and chemical parameters governing their efficiency in water splitting. It was found that some layered perovskites, such as $Sr_2Nb_2O_7$, $Sr_2Ta_2O_7$, and $La_2Ti_2O_7$, exhibit much higher photochemical activity, compared to their ABO_3 counterparts, while other layered structures, such as $Sr_3Ti_2O_7$, could be quite inactive [20].

RP-type nickelates, cobaltates, ferrites, and cuprates are also being investigated as advanced electrode or cathode materials for solid-oxide fuel cells [21] and metal-air batteries [22,23]. The propensity to reversibly absorb unusually large quantities of water molecules was also discovered in RP Ba_2ZrO_4 [24] and in homologous oxifluorides [25,26], as well as in a more complicated RP $PrSr_3Co_{1.5}Fe_{1.5}O_{10-\delta}$ system [27]. The same tendency with respect to CO_2 absorption was observed in a variety of perovskite-type or stoichiometrically related oxide compounds, such as RP $Li_2SrTa_2O_7$ and $LiHSrTa_2O_7$, β-K_2SO_4 orthotitanate Ba_2TiO_4 structure [28–30], or a 6H phase of $Ba_4Sb_2O_9$ [31]. These materials can be utilized as templates for the design of new functional-oxide membranes that could potentially greatly reduce the high energy costs associated with the process of CO_2 capture and storage [32], contributing to the already substantial efforts aimed at developing more advanced technologies for CO_2 sequestration.

In this work, a first-principles method, based on density-functional theory (DFT), is utilized to investigate electronic, vibrational, and dielectric properties of the RP Ba_2ZrO_4 structure, as well as its phase transformations under applied biaxial strain emulating epitaxial thin-film environment. We find that, for compressive strains ranging approximately from 1% to 3%, the system undergoes an incommensurate (IC) distortion characterized by the planar displacements of individual perovskite slabs away from their high symmetry positions. On the other hand, at tensile strains of above 3%, in-plane polar vibrational modes become unstable inducing a ferroelectric phase transformation that is accompanied by a divergence of the static dielectric response. It is remarkable, though, that *after the transition into the ferroelectric state* the in-plane dielectric permittivity remains unusually high (on the order of 300), which is explained by the presence of a Goldstone-like polarization-rotational excitation [33] in the system. Finally, we identify another, smaller anomaly in the in-plane static dielectric permittivity, which occurs near 1% compression, marking the transition between the IC and commensurate states of the Ba_2ZrO_4 structure.

II. METHODS

All the DFT-based first-principles calculations discussed below were performed using the QUANTUM ESPRESSO package (QE) [34]. The exchange correlation energy was evaluated within the local density approximation (LDA), using the Perdew-Zunger parametrization [35]. Electronic wave functions (density) were expanded in plane waves up to a kinetic energy cutoff of 30 Ry (300 Ry), while core and valence electrons were treated with Vanderbilt ultrasoft pseudopotentials [36]. Integrations over the Brillouin zone (BZ) of the RP Ba_2ZrO_4 structure were approximated by sums over the $6 \times 6 \times 2$ (shifted) Monkhorst-Pack (MP)[37] k-point mesh. In order to investigate the material structural stability and identify unstable phonon branches, phonon dispersions were computed across the BZ with the help of density-functional perturbation theory (DFPT) approach within QE [38], utilizing the $6 \times 6 \times 4$ (unshifted) MP mesh. All calculations, including lattice parameter and internal ionic position optimization, as well as the DFPT-based evaluation of phonon bands, were carried out for the tetragonal $P4/mmm$ cell containing two Ba_2ZrO_4 structural units (s.u.). In all cases, ionic forces were relaxed to less than 0.2×10^{-5} Ry bohr^{-1} ($\sim 0.5 \times 10^{-4}$ eV Å^{-1}) and the appropriate stress tensor components $\sigma_{\alpha\beta}$ (α and β are Cartesian directions x, y and z) were converged to values below 0.2 kbar. Ionic Wyckoff positions for the body-centered RP Ba_2ZrO_4 structure (space group $I4/mmm$) are provided in Table I. Calculations for cubic perovskite $BaZrO_3$ (space group $Pm\bar{3}m$) were performed under the same conditions, with the exception of the involved MP meshes that were rescaled along the z direction.

Epitaxial thin-film constraint on a cubic (001)-oriented substrate was simulated by varying the in-plane lattice constant a of the tetragonal cell and allowing the out-of-plane lattice constant c to relax (by converging the normal stress in this direction to a small value), while preserving the imposed $P4/mmm$ unit-cell symmetry. The associated biaxial misfit strain is defined as $\varepsilon_s = (a - a_0)/a_0$, where a_0 is the in-plane lattice parameter of the free standing Ba_2ZrO_4 structure with all the normal stress tensor components relaxed to less than 0.2 kbar. In order to evaluate long-range dipolar contribution to the lattice dynamics of the system, Born effective-charge tensors $Z^*_{i,\alpha\beta}$, where i is the ion number, and high-frequency dielectric permittivity tensor $\epsilon^{\infty}_{\alpha\beta}$ were calculated by utilizing

TABLE I. Structural parameters of the RP Ba_2ZrO_4 (space group $I4/mmm$) computed for various biaxial strains ε_s. Potential substrate assignments are indicated where possible.

Atom	Wyckoff positions	Symmetry	Coordinates
Zr	2(*a*)	$4/mmm$	0,0,0
O_x, O_y	4(*c*)	*mmm*	$\frac{1}{2}$,0,0; 0$\frac{1}{2}$,0
O_z	4(*e*)	4*mm*	0,0,$\pm z_{O_z}$
Ba	4(*e*)	4*mm*	0,0, $\pm z_{Ba}$
ε_s (%)	*a* (Å)	*c*/*a*	Substrate
−2.0	4.048	3.317	Mg_2AlO_4
−1.0	4.090	3.261	
−0.5	4.110	3.234	
0.0	4.131	3.207	$BaZrO_3$?
0.5	4.152	3.180	$BaZrO_3$?
1.0	4.172	3.154	
2.0	4.214	3.103	MgO
3.0	4.255	3.053	
3.5	4.276	3.029	

Experimental values ($I4/mmm$ structure at 500 °C) [24]

a (Å)	*c*/*a*
4.2046	3.232

Perovskite $Pm\bar{3}m$ $BaZrO_3$

	Ref. [44] (exp.)	This work	Refs. [45,46]
a (Å)	4.191	4.1542	4.166

the DFPT approach. These data were then used to compute phonon plasma frequencies $\Omega_{p,m}$ (here index *m* enumerates phonon modes) and static dielectric permittivity tensor $\epsilon^0_{\alpha\beta}$ following the schemes described in Refs. [39–42]. For all polar structures, a linearized approximation [43] involving products of $Z^*_{i,\alpha\beta}$ and ionic displacements away from their centrosymmetric positions was used to estimate the total electric polarization.

III. RESULTS AND DISCUSSION

A. Structural properties

In Table I, we list structural parameters for the high-symmetry (centrosymmetric) $I4/mmm$ phase of the RP Ba_2ZrO_4 under varying degrees of biaxial strain ε_s. Parameters computed at $\varepsilon_s = 0$ correspond to the case of the unit cell optimized for absent applied stresses, i.e., $\sigma_{\alpha\alpha} \to 0$ ($\sigma_{\alpha\beta} \equiv 0$ for $\alpha \neq \beta$ by symmetry). Experimental lattice constants for the ceramic sample at 500°C obtained by Shpanchenko and coworkers [24] are also shown for comparison and are, on average, underestimated by our DFT-based results by ∼2%. Finally, at the bottom of Table I, structural parameters for the perovskite $BaZrO_3$ are also presented. The calculated lattice constant for its cubic $Pm\bar{3}m$ phase is 4.154 Å and underestimates the experimental value (4.191 Å at 2 K) [44] by ∼1%, which is typical for DFT-LDA. This information shows that both experimentally and computationally estimated in-plane lattice constants of stress-free RP Ba_2ZrO_4 and cubic-perovskite $BaZrO_3$ are very close. Since the latter compound is nonpolar over a wide range of temperatures (that is, under no applied stress—but predicted to develop polar distortions under either tension, or compression) [47], it may potentially be utilized as a substrate material for the growth of Ba_2ZrO_4 thin films.

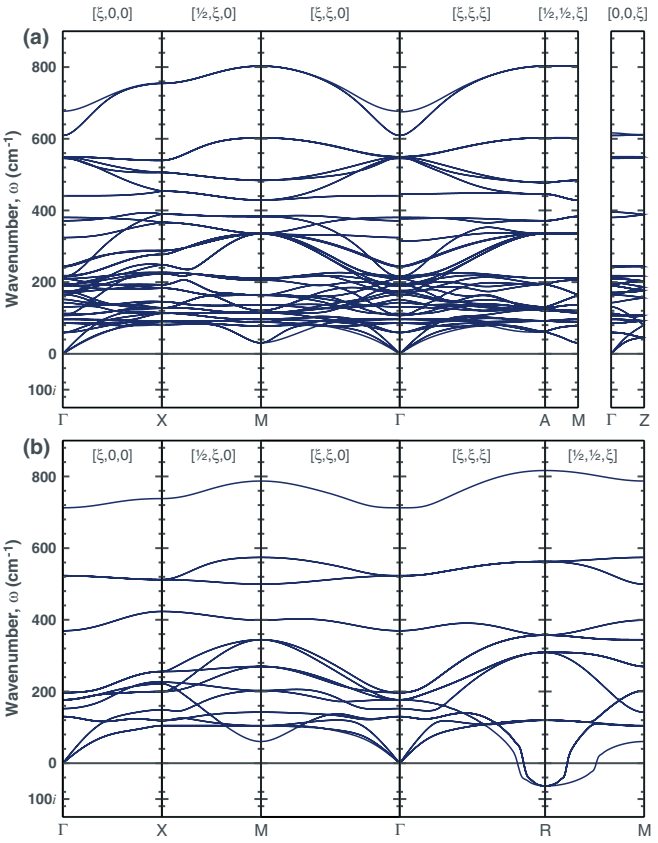

FIG. 2. (Color online) Phonon bands calculated for (a) $I4/mmm$ Ba_2ZrO_4 (calculation for the two s.u. cell of $P4/mmm$ symmetry) and (b) $Pm\bar{3}m$ $BaZrO_3$. Imaginary frequencies associated with unstable phonon modes are plotted below the zero line.

B. Vibrations and structural instability analysis

Phonon dispersion curves calculated for the stress-free $I4/mmm$ RP Ba_2ZrO_4 and $Pm\bar{3}m$ perovskite $BaZrO_3$ are depicted in Figs. 2(a) and 2(b), respectively. The phonon bands of the RP Ba_2ZrO_4 show no existing lattice instabilities—same as in RP Sr_2TiO_4; see, e.g., Fig. 2 in Ref. [48]—suggesting that this structure is stable as a bulk solid, which is in agreement with available experimental data for ceramic samples [24–26]. This is not the case for cubic perovskite $BaZrO_3$, which exhibits an instability around the R ($\frac{1}{2},\frac{1}{2},\frac{1}{2}$) point at the BZ boundary. This instability is antiferrodistortive (AFD) in character, with the octahedral cage rotation described by the $a^0b^-c^-$ Glazer tilt pattern [49]. Our results, shown in Fig. 2(b), are in good agreement with previous calculations [44–46,50–52] that also predict the condensation of the soft R_{25} phonon. However, experimental evidence of this instability is lacking, with perovskite $BaZrO_3$ remaining cubic and paraelectric down to the temperature of 2 K [44]. It was suggested that the source of this discrepancy may be due to quantum fluctuations that destroy the long-range order in rotational distortions of the oxygen octahedra and therefore prevent the freezing-in of the AFD instability [44]. An alternative explanation outlined in Refs. [45,46] proposes the existence

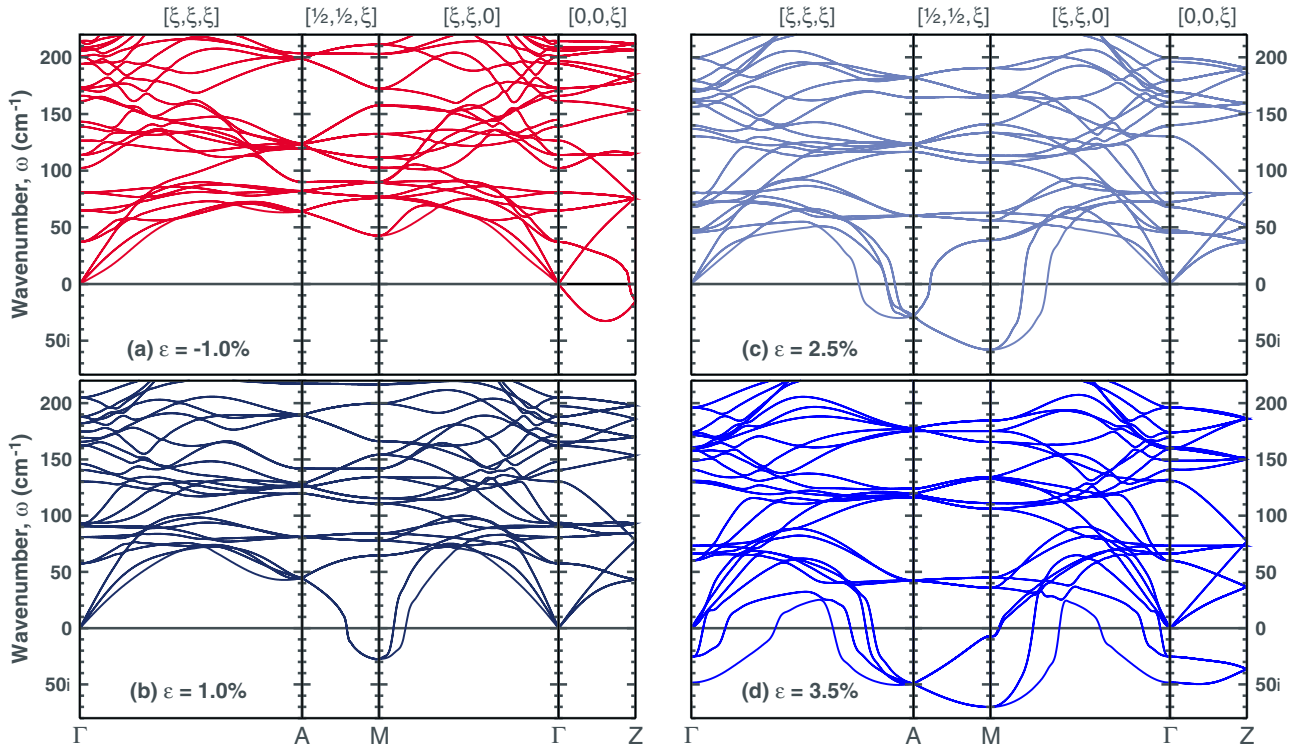

FIG. 3. (Color online) Phonon-band dispersions along some high-symmetry BZ directions in the tetragonal $P4/mmm$ unit cell of RP Ba_2ZrO_4 under 1% compression in (a), 1%, 2.5%, and 3.5% tension (b), (c), and (d). Imaginary frequencies associated with unstable phonon modes are plotted below the zero line. BZ intervals MA and ΓZ are not shown in proper scale to other intervals (unlike in Fig. 2) to show band dispersions along the z direction in greater detail.

of a variety of (dynamically stable) phases with different octahedral rotation patterns that form a glassy state, which looks cubic in diffraction, upon cooling.

Calculated phonon dispersion curves for the epitaxially strained $I4/mmm$ RP Ba_2ZrO_4 are shown in Fig. 3, including 1% biaxial compression in panel (a) and 1%, 2%, and 3.5% biaxial tension in panels (b), (c), and (d), respectively. The BZ path along which the phonon bands are depicted in the figure is chosen to highlight the changes in the structure's vibrational spectrum under varying strain, rather than for the sake of computational completeness. The omitted data do not change the conclusions presented in this section.

Under 1% to 2% compression, the dominant unstable phonon band is found in the vicinity of the $Z(0,0,\frac{1}{2})$ point and along the Γ-Z BZ direction [see Fig. 3(a)], although other, weaker instabilities are also present along the Γ-X and Γ-R lines (not shown here). Visualization of the eigenvectors of the unstable modes at Z identifies them as sliding of individual Ba_2ZrO_4 slabs with respect to each other in the xy plane that may also be accompanied by distortions within the outlying (rocksalt) BaO monolayers. Remarkably, the maximum strength (indicated by the largest value of the imaginary frequency $\sim 32i$ cm^{-1}) of the lowest unstable band is attained at a $\mathbf{q}$ point within the Γ-Z interval, rather than at the BZ edge or center. Since such $\mathbf{q}$ points do not usually correspond to an integer number of Ba_2ZrO_4 unit cells, this mode describes an IC modulation of the $I4/mmm$ high-symmetry state of the RP compound. The nature of the IC distortions that occur in the RP Ba_2ZrO_4 in biaxial compression is discussed in detail below, in Sec. III C.

Under epitaxial tension, lattice instabilities emerge at the M point at $\varepsilon_s \simeq 1\%$ and then deepen as the degree of strain increases [see Figs. 3(b) and 3(c)]. At $\varepsilon_s \simeq 2.5\%$, other instabilities appear at the Γ and A point and persist for higher tensile strains. At 3.5% tension, large instability regions form along the Γ–A–M–Γ–Z path in the BZ [see Fig. 3(d)], as well as—less prominently—along other directions. Most of these instabilities are AFD in character, while others are ferroelectric. The AFD distortion at the M point can be described as a combination of the $a^-b^0c^0$ and $a^0b^-c^0$ Glazer tilt patterns that occur within the two neighboring Ba_2ZrO_4 perovskite slabs, respectively. The distortion at the A-point includes the $a^-b^-c^0$ Glazer tilt pattern within one of the two neighboring slabs and no rotations ($a^0b^0c^0$) in the other. Atomic-level animations for these vibrational modes at different levels of epitaxial strain are included as a Supplemental Material [53]. The influence of the latter on the functional properties of Ba_2ZrO_4 is further discussed in Sec. III D.

C. Incommensurate distortions

In this discussion, we follow the outline established in Ref. [48], where we have investigated the emergence of IC distortions in (as of now, fictitious) RP-type Ba_2TiO_4, also presenting a brief history of the studies of IC phases in insulators. Such states had been observed in a variety of dielectric materials, including a few compounds that are ferroelectric [54–56]. General theory elucidating the origins

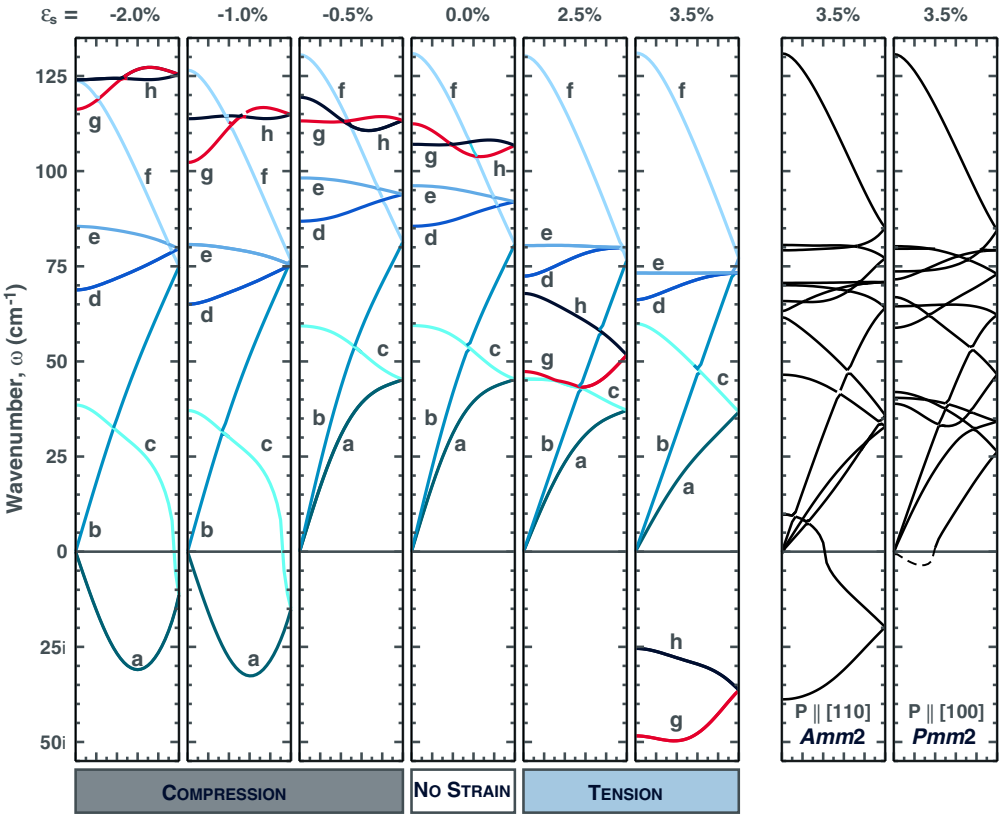

FIG. 4. (Color online) Evolution of the low-lying Γ-Z phonon bands in the epitaxial $I4/mmm$ RP Ba_2ZrO_4 structures with respect to varying biaxial strain ε_s. Imaginary frequencies associated with unstable modes are plotted as negative numbers below the horizontal zero line. See Table II for the band symmetry assignments. Phonon bands for the polar structures at $\varepsilon_s = 3.5\%$, with polarization along [110] and [100] directions, are shown in the two rightmost panels.

of IC distortions in insulators is due to Heine and McConnell [57,58]. For the sake of completeness, here we reiterate its most important conclusions.

IC distortions arise from interactions between two or more different transformation modes—displacive (i.e., phonons) or otherwise in character—in the undistorted state of the system at the temperature above the IC phase transition. For an IC ground state to become possible, the mode symmetries should be different at a high-symmetry $\mathbf{q}$ point $\tilde{\mathbf{q}}$ (e.g., BZ center or edge), prohibiting mode interaction at this point, but become the same at more generic points within the vicinity of $\tilde{\mathbf{q}}$, which allows the modes to interact. Similarly to hybridized electronic states of the same symmetry, such interaction bends the upper phonon band up and the lower band down, with the shape of the latter developing a downward "hump" with a minimum at a generic value of $\mathbf{q} \neq \tilde{\mathbf{q}}$. For close mode frequencies, this effect may be strong enough to push the minimum of the lower band below the zero line, producing an IC structural instability, such as the one shown in Fig. 3(a). The most simple connection between the interacting modes symmetries requires them to be either even, or odd with respect to some operation (e.g., an inversion center) belonging to the symmetry group of $\tilde{\mathbf{q}}$.

In Fig. 4, we present the evolution of the low-frequency phonon bands along the Γ-Z path within the ($P4/mmm$) BZ of the $I4/mmm$ RP Ba_2ZrO_4 as a function of epitaxial strain, ranging from 2.0% compression to 3.5% tension. Other BZ regions containing weaker instabilities are not shown, but their behavior could be analyzed following the same procedure. Atomic-level animations for some vibrations (or combinations thereof) belonging to the phonon bands considered here are included as a Supplemental Material [53]. In the accompanying Table II, we show the symmetries of the phonon bands identified in Fig. 4 at $\mathbf{q}$ points Γ, Z, and $\Lambda \in (\Gamma, Z)$. From this table and Fig. 4, the pair of doubly degenerate phonon bands denoted as **a** and **c** can be identified as the one satisfying the symmetry relation of Heine and McConnell for the formation of an IC state, which occurs under biaxial compression of more than 1%. The

TABLE II. (Color online) Phonon band symmetries along the Γ-Z path in the in the Brillouin zone of the $P4/mmm$ unit cell of the RP Ba_2ZrO_4.

Bands in Fig. 4		Γ (0,0,0) $4/mmm$	Λ (0,0,ξ) $4mm$	Z (0,0,$\frac{1}{2}$) $4/mmm$
a (teal)	(—)	E_u	E	E_u
b (light teal)	(—)	A_{2u}	A_1	A_{1g}
c (cyan)	(—)	E_u	E	E_g
d (blue)	(—)	E_g	E	E_g
e (sky blue)	(—)	E_g	E	E_u
f (light blue)	(—)	E_u	A_1	A_{2u}
g (red)	(—)	E_u	E	E_u
h (navy)	(—)	E_u	E	E_g

associated phonon modes transform according to irreps E_u and E_g, respectively, at Z, and irrep E at Λ. Visualization of phonon-mode eigenvectors at Z shows that these distortions correspond to individual Ba_2ZrO_4 slabs sliding against each other in the xy plane, with displacement patterns that are either odd (branch **a**), or even (branch **c**) with respect to an inversion through the center of the tetragonal $P4/mmm$ unit cell doubled along the [001] direction. Mode eigenvector analysis for *commensurate* values of ξ (see BZ-path markings on top of both panels in Fig. 3), equivalent to supercells made up of three, four, and five unit cells stacked along [001], produces displacement motifs that resemble mixtures of the pure E_u and E_g modes at Z. At $\varepsilon_s \geqslant -1\%$, the lower phonon branch **a** remains unstable for every nonzero value of ξ along the Λ–Z path, forming a minimum at $\xi_{\min} = \frac{3}{10} + \delta$ ($\delta > 0$ for all strains), while the upper branch **c** is stable throughout the same interval, with the exception of the vicinity of **q** point Z.

The other pair of phonon branches **g** and **h** that also satisfies the symmetry criteria of Heine and McConnell becomes unstable at biaxial tensions of above 3.0%. Their associated phonon modes transform in exactly the same fashion at point Z, and along the Λ–Z path, as those of the already considered branches **a** and **c** (see Table II). Examination of the phonon-mode eigenvectors of branches **g** and **h** at Γ point reveals that their displacement motifs are dominated by planar off-centrings of Ba ions within their cuboctahedral oxygen cages. Although Ba displacements are not accompanied by any significant off-centrings of Zr in their respective cages, we can still quantify these modes as polar distortions of the two Ba_2ZrO_4 slabs within the $P4/mmm$ unit cell, which are parallel (ferroelectric) for branch **g** and antiparallel (antiferroelectric) for branch **h**. At $\varepsilon_s \geqslant 3.5\%$, the lower branch **g** forms a shallow minimum at the value of $\xi_{\min}$ that is close, but not exactly equal, to $\frac{1}{4}$, which may potentially correspond to an IC modulation of the underlying $I4/mmm$ crystal structure. However, as shown in panel (d) of Fig. 3, at large tensile strains polar instabilities are weaker than the AFD ones at M and A points, and, therefore, without further considerations it is unclear whether or not the low-T ground state of the system is going to have any IC-polar character.

The rightmost panels of Fig. 4 depict the Γ–Z low-frequency phonon bands in the RP Ba_2ZrO_4 structure under 3.5% tensile biaxial strain where the $I4/mmm$ symmetry is broken by allowing planar polar distortions. These configurations were obtained by introducing the ionic distortions corresponding to the (doubly degenerate) phonon-mode eigenvectors of branch **g** at Γ point along the [110] and [100] directions, resulting in $Amm2$ and $Pmm2$ symmetries, respectively, and then relaxing the ionic forces and cell stress-tensor components under the same epitaxial strain constraint. The examination of the phonon bands reveals that the preferred polarization direction in plane is along [100], as the $Pmm2$ structure exhibits only a shallow instability (that may possibly be an artifact of the BZ sampling), while the $Amm2$ structure polarized along [110] remains highly unstable.

Summarizing the results discussed in this and in the previous subsections, we can establish a tentative phase diagram for the RP Ba_2ZrO_4 structure with respect to varying epitaxial strain ε_s. This diagram, presented in Fig. 5, shows the evolution of soft vibrational-mode frequencies ω at Γ and various BZ-boundary **q** points under changing ε_s.

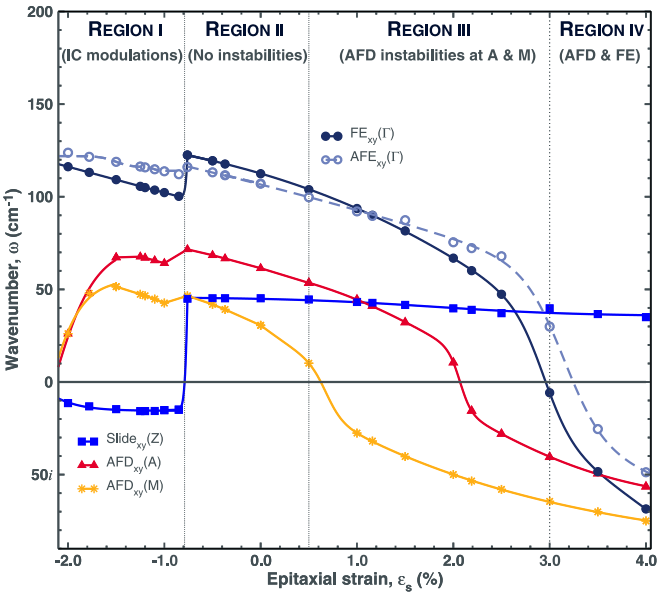

FIG. 5. (Color online) Soft vibrational modes frequencies ω at Γ and various BZ-boundary **q** points as functions of epitaxial strain ε_s for Ba_2ZrO_4.

We can separate the phase space for the system into four main regions according to the values of ε_s: (I) high compressions of above 0.8%–1.0%, dominated by IC distortions; (II) moderate compressions and tensions, where the nonpolar $I4/mmm$ structure is stable; (III) intermediate tensions ranging from 0.5 to ~3.0%, dominated by combinations of AFD distortions; (IV) high tensions of above 3.0%–3.5%, with polar distortions being of similar or greater strength than the AFD ones. Naturally, more work (currently in progress) is needed to unequivocally establish the stable structural configurations for Ba_2ZrO_4 for the specific values of epitaxial strain. However, comparing this situation to the case of the RP Ba_2TiO_4 that was studied before [48], we point out the greater complexity of the latter, with IC distortions persisting throughout the whole interval of considered strains and different kinds of IC distortions being possible, as well as their mixing with polar distortions.

D. Dielectric properties

The data presented in Fig. 5 indicates that the $I4/mmm$ configuration is stable only within a narrow interval of epitaxial strains (region II). Furthermore, the polar $Pmm2$ configuration is unstable with respect to AFD distortions (in region IV). We further attempt to trace the evolution of the dielectric properties of the RP Ba_2ZrO_4 structure for all the strain states included in this tentative phase diagram. According to the prescriptions for evaluating the (electronic and vibrational contributions to) static dielectric permittivity tensor $\epsilon^0_{\alpha\beta}$ [39–42], the required ingredients include ionic Born effective-charge tensors $Z^*_{i,\alpha\beta}$, high-frequency dielectric permittivity tensor $\epsilon^\infty_{\alpha\beta}$ and the set of the dynamical matrix eigenvalues and eigenvectors $\{\omega^2_m, \eta_m\}$

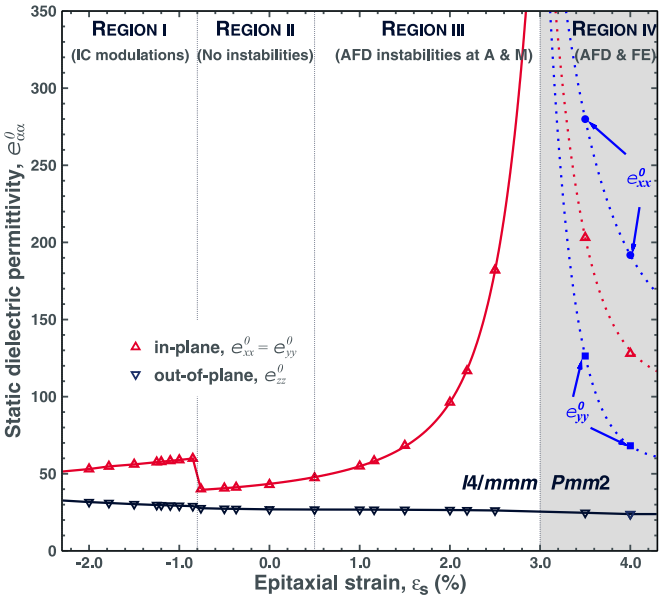

FIG. 6. (Color online) In- and out-of-plane components of the static dielectric permittivity tensor $\epsilon^0_{\alpha\alpha}$ computed for the RP Ba_2ZrO_4 structure with respect to varying biaxial strain ε_s. For all compressions and for tensions of less than 3.0%, the dielectric tensors are computed for the nonpolar $I4/mmm$ configuration, while for larger tensions they are computed for the polar $Pmm2$ configuration (where ϵ^0_{xx} and ϵ^0_{yy} are no longer equal by symmetry). Connecting lines are used to guide the eye.

at the BZ center, i.e.,

$$\epsilon^0_{\alpha\beta} = \epsilon^\infty_{\alpha\beta} + \sum_m \Delta\epsilon_{m,\alpha\beta}, \tag{1}$$

where $\Delta\epsilon_m$ is the contribution from vibrational mode m:

$$\Delta\epsilon_m \sim \frac{\Omega^2_{p,m}}{\omega^2_m} \tag{2}$$

and

$$(\Omega_{p,m})_\alpha \sim \sum_{i,\gamma} Z^*_{i,\alpha\gamma}\eta_m(i,\gamma). \tag{3}$$

These equations remain valid even for systems with structural instabilities as long as there are no unstable (i.e., $\omega^2_m \leqslant 0$) modes at the Γ point that have substantial plasma frequencies $\Omega_{p,m}$. Therefore, omitting the influence of IC or AFD distortions, the static dielectric permittivity can be evaluated for the $I4/mmm$ structure for all the considered compressive strains and for tensile strains of up to ~3%. At larger tensile strains, when the Γ-point polar distortions become unstable in the $I4/mmm$ structure, the polarized $Pmm2$ structure that contains no Γ-point instabilities (see rightmost panels in Fig. 4) can be used for the same purpose.

The in-plane and out-of-plane components of the static dielectric permittivity tensor $\epsilon^0_{\alpha\alpha}$ computed for the RP Ba_2ZrO_4 structure under these conditions are presented in Fig. 6. At ~3% biaxial tension, where the tentative $I4/mmm$ to $Pmm2$ transition occurs as the vibrational frequency of the $FE_{xy}(\Gamma)$ mode goes to zero (see Fig. 5), there is a divergence of the in-plane component of the dielectric permittivity tensor, while its out-of-plane component remains continuous. Furthermore, at the boundary between regions I and II ($\varepsilon_s \simeq -0.9\%$), we observe another, more mild anomaly in the in-plane dielectric permittivity tensor component behavior, which happens due to a lock-in transition out of the IC state. For all the considered epitaxial conditions, with the exception of tensions greater than 1.5%, the values of both in- and out-of-plane dielectric permittivity tensor components remain very similar to those of $BaZrO_3$, which usually range from 40 to 60 [44,45,47,51,59].

Table III displays the diagonal components of the Born effective charge tensors and the high-frequency dielectric permittivity tensors $\epsilon^\infty_{\alpha\alpha}$ calculated for the $I4/mmm$ Ba_2ZrO_4 configuration under a variety of biaxial epitaxial strains. Furthermore, in Table IV, we present the same information for the polar $Pmm2$ and $Amm2$ Ba_2ZrO_4 configurations at $\varepsilon_s = 3.5\%$, as well as for the relaxed $Pm\bar{3}m$ cubic $BaZrO_3$. In all of the Ba_2ZrO_4 structures, we observe anomalously large effective charges, compared to their nominal values. This effect is especially pronounced for the Z^*_{xx} and Z^*_{yy} components of the charge tensors of Zr and equatorial oxygens, but tends to diminish slightly under increasing tensile strains. Similar results for the Born effective charges behavior under applied epitaxial strain were obtained for $BaZrO_3$ [47].

The plasma frequencies, $\Omega_{p,m}$, and contributions to the static dielectric tensor, $\Delta\epsilon_m$, for the IR-active vibrational modes, ω_m, computed for the RP Ba_2ZrO_4 structure under changing biaxial epitaxial strains are collected in Table V. The polar, $Pmm2$, configuration was used at high tensions, while nonpolar, $I4/mmm$, was employed for all other strains. At moderate strains far away from the nonpolar-to-polar phase transition (regions I through III) individual mode contributions

TABLE III. Ionic Born effective-charge tensors $Z^*_{i,\alpha\beta}$ and high-frequency dielectric permittivity tensors $\epsilon^\infty_{\alpha\alpha}$ computed for the $I4/mmm$ RP Ba_2ZrO_4 structures at various values of biaxial strain ε_s. Here, i is the ion number, α and β are Cartesian directions x, y, and z.

ε_s (%)	−1.0%			0.0%			1.0%			2.0%			3.5%		
Atom	Z^*_{xx}	Z^*_{yy}	Z^*_{zz}	Z^*_{xx}	Z^*_{yy}	Z^*_{zz}	Z^*_{xx}	Z^*_{yy}	Z^*_{zz}	Z^*_{xx}	Z^*_{yy}	Z^*_{zz}	Z^*_{xx}	Z^*_{yy}	Z^*_{zz}
Zr	6.00	6.00	5.08	5.92	5.92	5.17	5.85	5.85	5.26	5.77	5.77	5.33	5.66	5.66	5.46
O_x	−4.72	−2.07	−1.84	−4.65	−2.09	−1.83	−4.59	−2.11	−1.82	−4.53	−2.14	−1.81	−4.45	−2.17	−1.78
Ba	2.54	2.54	2.97	2.52	2.52	3.00	2.50	2.50	3.02	2.48	2.48	3.04	2.45	2.45	3.08
O_z	−2.20	−2.20	−3.73	−2.16	−2.16	−3.81	−2.12	−2.12	−3.89	−2.08	−2.08	−3.96	−2.02	−2.02	−4.08
$\epsilon^\infty_{\alpha\alpha}$	(4.53, 4.53, 4.66)			(4.51, 4.51, 4.67)			(4.48, 4.48, 4.68)			(4.46, 4.46, 4.70)			(4.42, 4.42, 4.72)		

TABLE IV. Ionic Born effective-charge tensors $Z^*_{i,\alpha\beta}$ and high-frequency dielectric permittivity tensors $\epsilon^{\infty}_{\alpha\alpha}$ computed for the relaxed $Pm\bar{3}m$ $BaZrO_3$ and polar configurations of RP Ba_2ZrO_4 structures at 3.5% biaxial tensile strain. Here i is the ion number, α and β are Cartesian directions x, y and z. For the polar Ba_2ZrO_4 structures, components P_α of the total polarization vector **P**, given in C/m^2, are presented in the last row of the table [60].

Atom	$BaZrO_3$ ($Pm\bar{3}m$)			Ba_2ZrO_4 ($Pmm2$)			Ba_2ZrO_4 ($Amm2$)		
	Z^*_{xx}	Z^*_{yy}	Z^*_{zz}	Z^*_{xx}	Z^*_{yy}	Z^*_{zz}	Z^*_{xx}	Z^*_{yy}	Z^*_{zz}
Zr	6.09	6.09	6.09	5.65	5.60	5.38	5.63	5.63	5.39
O_x	−2.05	−4.81	−2.05	−4.44	−2.17	−1.78	−4.43	−2.17	−1.78
Ba	2.74	2.74	2.74	2.47	2.45	3.06	2.46	2.46	3.06
O_z	−2.05	−2.05	−4.81	−2.04	−2.01	−4.03	−2.02	−2.02	−4.04
$\epsilon^{\infty}_{\alpha\alpha}$	(4.90, 4.90, 4.90)			(4.43, 4.41, 4.69)			(4.42, 4.42, 4.70)		
P_α				(0.000, 0.121, 0.000)			(0.076, 0.076, 0.000)		

to the dielectric tensor remain modest. On the other hand, the observed large (∼100 and above) contributions from polar modes in the $Pmm2$ structure at large tensions are surprising. Typically, such contributions are encountered in the nonpolar centrosymmetric configuration close to the polar phase transition, which is accompanied by freezing-in of the FE(Γ) structural distortion that has high plasma frequency. But after transitioning into the polar state this distortion becomes strongly locked along some crystallographic direction and thus cannot easily change its phase or amplitude. As a result, the associated high-plasma-frequency vibrational modes that change the direction and/or amplitude (or modulus) of the polarization vector are stiffened considerably and cannot contribute much to the static dielectric constant [see Eq. (2) above]. Remarkably, we find this not to be the case in the $Pmm2$ Ba_2ZrO_4 structure at $\varepsilon_s \simeq 3.5\%$. As shown in Fig. 6, the in-plane component of the dielectric tensor *does not diminish* following the transition into the polar configuration with the frozen-in $FE_{xy}(\Gamma)$ distortion.

E. The mystery of high dielectric response in the polar phase

To investigate the issue, we have sampled the energy landscape of the system under high tensions ($\varepsilon_s \geqslant 3.0\%$) with respect to this distortion. Since the $FE_{xy}(\Gamma)$ vibrational mode is doubly degenerate (transforms according to the E_u irrep), potentially any linear combination of the two associated eigenvectors, $\eta^{\mathrm{FE}}_x = Q_x\hat{\mathbf{e}}_x$ and $\eta^{\mathrm{FE}}_y = Q_y\hat{\mathbf{e}}_y$, could condense during the transition from the paraelectric $I4/mmm$ phase to a polar phase with reduced symmetry. Taking the $I4/mmm$ structure as a starting point, we computed the energies of configurations with frozen in combinations of η^{FE}_x and η^{FE}_y distortions whose amplitudes Q_x and Q_y were varied on a 15×15 square grid. The resulting energy surface is shown in Fig. 7. Its minima are located at $|\mathbf{Q}| = Q_x \simeq 6.0\%a$ along the [100] and symmetrically equivalent crystallographic directions, which is consistent with the $Pmm2$ polar configuration being most stable. On the other hand, it also has saddle points at approximately the same value of $|\mathbf{Q}| = \sqrt{Q_x^2 + Q_y^2}$, $Q_x = Q_y$, along the [110] and symmetrically equivalent crystallographic directions, i.e., for the frozen-in distortion that results in the emergence of the unstable $Amm2$ polar structure. The linearized estimate for the total polarization[43] produces similar values for both highly-symmetric polar states: $P(Pmm2) = 0.121\,\mathrm{C/m^2}$ and $P(Amm2) = 0.108\,\mathrm{C/m^2}$. A closer examination of the shape of the energy minima for the surface in Fig. 7 shows that they are rather shallow—$|E(Pmm2) - E(Amm2)| = 0.44$ meV, while $|E(Pmm2) - E(I4/mmm)| = 1.67$ meV—and elongated, or trenchlike in

TABLE V. Phonon plasma frequencies $\Omega_{p,m}$ and contributions to the static dielectric tensor $\Delta\epsilon_m$ in RP Ba_2ZrO_4 at various values of biaxial strain ε_s. Both vibrational and plasma frequencies are given in cm^{-1}. Mode symmetry assignments on the right refer to the polar $Pmm2$ configuration at $\varepsilon_s = 3.5\%$, while those on the left are valid for the nonpolar $I4/mmm$ configuration used in the calculations for all the other strain states presented in this table.

ε_s (%)	−1.0%			0.0%			1.0%			2.0%			3.5% ($Pmm2$)			ε_s (%)
Mode	ω_m	$\Omega_{p,m}$	$\Delta\epsilon_m$	ω_m	$\Omega_{p,m}$	$\Delta\epsilon_m$	ω_m	$\Omega_{p,m}$	$\Delta\epsilon_m$	ω_m	$\Omega_{p,m}$	$\Delta\epsilon_m$	ω_m	$\Omega_{p,m}$	$\Delta\epsilon_m$	Mode
E_u	102	676	43.65	112	608	29.28	94	609	42.25	67	613	104.62	39	637	267.93	B_2
A_{2u}	171	666	15.23	171	648	13.73	172	646	14.15	170	643	14.41	59	628	113.56	A_1
E_u	209	642	9.47	217	611	7.86	223	579	6.72	226	572	6.36	169	616	13.24	B_1
A_{2u}	307	858	7.83	324	851	6.89	338	838	6.15	350	816	5.32	225	560	6.19	B_2
A_{2u}	435	543	1.56	441	568	1.66	446	595	1.78	451	628	1.98	233	570	5.98	A_1
E_u	585	659	1.27	550	604	1.21	516	569	1.22	484	523	1.15	365	748	4.20	B_1
$\epsilon^0_{\alpha\alpha}$	(58.9, 58.9, 29.3)			(43.0, 43.0, 26.9)			(54.9, 54.9, 26.8)			(96.3, 96.3, 26.5)			(279.9, 126.3, 25.6)			$\epsilon^0_{\alpha\alpha}$

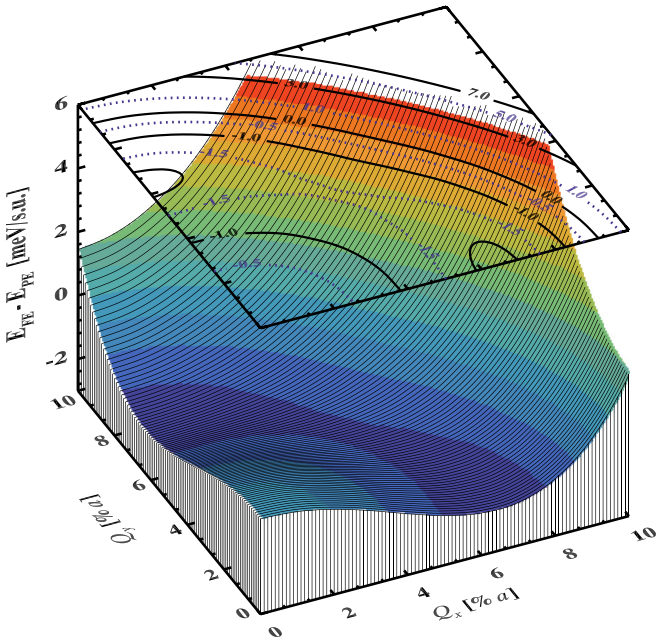

FIG. 7. (Color online) Energy landscape for the $I4/mmm$ RP Ba_2ZrO_4 structure under 3.5% epitaxial tension with a frozen-in doubly degenerate FE_{xy} distortion. Q_x and Q_y are the amplitudes of the mode eigenvectors η_x^{FE} and η_y^{FE} polarized along the x and y axes, respectively. The energy of the paraelectric $I4/mmm$ phase is taken as zero and a is the value of the in-plane lattice parameter.

the direction perpendicular to the one of the polarization vector. Animation of the ionic displacements produced by the vibrational mode that contributes the most to the dielectric permittivity tensor in the $Pmm2$ configuration at $\varepsilon_s = 3.5\%$ (B_2 mode with $\omega = 39\,\mathrm{cm}^{-1}$ and $\Delta\epsilon = 268$; see rightmost entry in Table V and Ref. [53]) reveals that this mode corresponds to in-plane libration of the polarization vector within the trenchlike energy landscape. Therefore we can conclude that, while after the transition into the $Pmm2$ configuration the amplitude of the polarization vector becomes fixed, its direction (or phase) can still be easily changed, which gives rise to the observed large value of the dielectric constant. This behavior is very similar to the one we have observed before in the RP $PbSr_2Ti_2O_7$ (PSTO) superlattice, which exhibits an in-plane Goldstone-like (or a phason) [61,62] polar excitation [33]. Although the shape of the presented energy surface for Ba_2ZrO_4 is not as round as in PSTO (compare with Fig. 2(a) in Ref. [33]), we could still speculate that by further fine-tuning the value of applied epitaxial strain the energy difference between the $Pmm2$ and $Amm2$ states can be minimized, resulting in a better "mexican hat" energy landscape.

Recognizing the outlined common trends in transitional behavior of RP Ba_2ZrO_4 and PSTO, it is, nevertheless, even more interesting to consider the differences between these two systems. Although the Goldstone-like excitation in PSTO was predicted to occur at low epitaxial strains, due to its structural complexity, as of now this material has yet to be synthesized. Molecular beam epitaxy has been identified as the most likely technique capable of producing this superlattice, however, the presence of lead still poses a great challenge to achieving successful growth of PSTO [63]. Furthermore, our previous investigations [33,64] identify the relative insensitivity of Pb^{2+} energetics towards a particular direction of the polar distortion as an essential component required for inducing Goldstone-like excitations. On the other hand, RP Ba_2ZrO_4 has been already produced as a ceramic [24–26]. There should be, in principle, no unsurmountable obstacles to fabricating it in the thin-film form, although the predicted Goldstone-like behavior requires high tensions on square substrates with a spacing of about 4.2–4.3 Å, which may be hard to achieve, both due to the absence of suitable substrates and very low critical thickness for the coherent film growth under such high strain. In addition, special measures will have to be taken to control the influence of AFD instabilities that may compete against the FE distortions, swaying the ground state of the system towards a nonpolar one. Finally, Ba_2ZrO_4 contains no lead or other lone-pair active ions, and thus it is currently unclear exactly what kind of mechanism—on the level of underlying electronic structure—is actually responsible for the emergence of Goldstone-like excitations in it.

IV. CONCLUSIONS

We have employed a first-principles approach based on DFT to study electronic, vibrational and dielectric properties of the RP-type layered oxide Ba_2ZrO_4, as well as its phase transformations under applied biaxial strain emulating epitaxial thin-film environment. Since this compound exhibits a yet poorly understood affinity for trapping small molecules, such as water and CO_2 [24–26], it may be valuable to achieve a better understanding of its functional behavior, with an aim of creating novel materials where processes of molecular absorption and desorption could be controlled on nanoscale.

Our investigation shows that the tentative phase space for the epitaxial RP Ba_2ZrO_4 can be separated into four main regions according to the values of the applied strain ε_s: (I) IC distortions at high compressions of above 0.8%–1.0%; (II) centrosymmetric $I4/mmm$ structure at moderate compressions and tensions; (III) structure modulated by AFD oxygen-cage rotations at intermediate tensions ranging from 0.5% to ~3.0%; (IV) structure modulated by both AFD and FE distortions at high tensions of above 3.0%–3.5%.

Remarkably, though, after the transition from the centrosymmetric state into the polar $Pmm2$ state, the in-plane dielectric permittivity remains unusually high (on the order of 300). We explain that by the predisposition of the polar configuration towards developing Goldstone-like excitations that are manifested through easy librations of the in-plane polarization away from its minimum-energy crystallographic direction. Although at the strains considered so far the circular groove in the energy landscape is not as pronounced here as in the case of $PbSr_2Ti_2O_7$ RP superlattice [33], we still observe shallow energy minima that are extended in the direction perpendicular to that of the minimum-energy polarization vector ([100] and symmetrically equivalent directions in the $Pmm2$ structure) that allow for the emergence of polar-phason instabilities. The nature of such excitations in the RP Ba_2ZrO_4 structure—which, unlike the previously studied one, does not

contain lead or other lone-pair active ions—is currently unclear and the work to elucidate their origins, as well as to find ways to tune out the competing AFD instabilities, is currently underway.

ACKNOWLEDGMENTS

L.L. acknowledges Krishna Pitike for insightful discussions on symmetry and William Parker for his help on the technicalities of QUANTUM ESPRESSO.

[1] M. Misono, *Heterogeneous Catalysis of Mixed Oxides: Perovskite and Heteropoly Catalysts* (Elsevier Science, Burlington, 2013).
[2] R. V. Wang, D. D. Fong, F. Jiang, M. J. Highland, P. H. Fuoss, C. Thompson, A. M. Kolpak, J. A. Eastman, S. K. Streiffer, A. M. Rappe, and G. B. Stephenson, Phys. Rev. Lett. **102**, 047601 (2009).
[3] M. J. Highland, T. T. Fister, M.-I. Richard, D. D. Fong, P. H. Fuoss, C. Thompson, J. A. Eastman, S. K. Streiffer, and G. B. Stephenson, Phys. Rev. Lett. **105**, 167601 (2010).
[4] M. J. Highland, T. T. Fister, D. D. Fong, P. H. Fuoss, C. Thompson, J. A. Eastman, S. K. Streiffer, and G. B. Stephenson, Phys. Rev. Lett. **107**, 187602 (2011).
[5] R. Herger, P. R. Willmott, O. Bunk, C. M. Schlepütz, B. D. Patterson, and B. Delley, Phys. Rev. Lett. **98**, 076102 (2007).
[6] A. M. Kolpak, D. Li, R. Shao, A. M. Rappe, and D. A. Bonnell, Phys. Rev. Lett. **101**, 036102 (2008).
[7] D. M. Kienzle, A. E. Becerra-Toledo, and L. D. Marks, Phys. Rev. Lett. **106**, 176102 (2011).
[8] K. Aleksandrov and V. Beznosikov, Phys. Solid State **39**, 695 (1997).
[9] R. Mitchell, *Perovskites: Modern and Ancient* (Almaz Press, Ontario, 2002).
[10] R. E. Schaak and T. E. Mallouk, Chem. Mater. **14**, 1455 (2002).
[11] K. G. Sanjaya Ranmohotti, E. Josepha, J. Choi, J. Zhang, and J. B. Wiley, Adv. Mater. **23**, 442 (2011).
[12] K. Domen, J. Yoshimura, T. Sekine, A. Tanaka, and T. Onishi, Catal. Lett. **4**, 339 (1990).
[13] M. Machida, K. Miyazaki, S. Matsushima, and M. Arai, J. Mater. Chem. **13**, 1433 (2003).
[14] K.-i. Shimizu, Y. Tsuji, T. Hatamachi, K. Toda, T. Kodama, M. Sato, and Y. Kitayama, Phys. Chem. Chem. Phys. **6**, 1064 (2004).
[15] S. Nishimoto, M. Matsuda, and M. Miyake, J. Solid State Chem. **178**, 811 (2005).
[16] I. Rodionov, O. Silyukov, and I. Zvereva, Russ. J. Gen. Chem. **82**, 635 (2012).
[17] I. Rodionov, O. Silyukov, T. Utkina, M. Chislov, Y. Sokolova, and I. Zvereva, Russ. J. Gen. Chem. **82**, 1191 (2012).
[18] J. Lee, Catal. Surv. Asia **9**, 217 (2005).
[19] G. Centi and S. Perathoner, Microporous Mesoporous Mater. **107**, 3 (2008).
[20] J. Kim, D. Hwang, H. Kim, S. Bae, J. Lee, W. Li, and S. Oh, Top. Catal. **35**, 295 (2005).
[21] A. Tarancon, M. Burriel, J. Santiso, S. J. Skinner, and J. A. Kilner, J. Mater. Chem. **20**, 3799 (2010).
[22] T. Takeguchi, T. Yamanaka, H. Takahashi, H. Watanabe, T. Kuroki, H. Nakanishi, Y. Orikasa, Y. Uchimoto, H. Takano, N. Ohguri, M. Matsuda, T. Murota, K. Uosaki, and W. Ueda, J. Am. Chem. Soc. **135**, 11125 (2013).
[23] K.-N. Jung, J.-H. Jung, W. B. Im, S. Yoon, K.-H. Shin, and J.-W. Lee, ACS Appl. Mater. Interfaces **5**, 9902 (2013).
[24] R. V. Shpanchenko, E. V. Antipov, and L. M. Kovba, Materials Science Forum **133-136**, 369 (1993).
[25] P. R. Slater and R. K. B. Gover, J. Mater. Chem. **11**, 2035 (2001).
[26] P. R. Slater and R. K. B. Gover, J. Mater. Chem. **12**, 291 (2002).
[27] L. Jantsky, H. Okamoto, A. Demont, and H. Fjellvåg, Inorg. Chem. **51**, 9181 (2012).
[28] H. Marusawa and Y. Saito, Key Eng. Mater. **350**, 143 (2007).
[29] Y. Saito, H. Sato, and Y. Sakabe, J. Chem. Eng. Jpn. **41**, 441 (2008).
[30] R. Inoue, S. Ueda, K. Wakuta, K. Sasaki, and T. Ariyama, ISIJ Int. **50**, 1532 (2010).
[31] M. T. Dunstan, W. Liu, A. F. Pavan, J. A. Kimpton, C. D. Ling, S. A. Scott, J. S. Dennis, and C. P. Grey, Chem. Mater. **25**, 4881 (2013).
[32] D. M. D'Alessandro, B. Smit, and J. R. Long, Angew. Chem. Int. Ed. **49**, 6058 (2010).
[33] S. M. Nakhmanson and I. Naumov, Phys. Rev. Lett. **104**, 097601 (2010).
[34] P. Giannozzi, S. Baroni, N. Bonini, M. Calandra, R. Car, C. Cavazzoni, D. Ceresoli, G. L. Chiarotti, M. Cococcioni, I. Dabo, A. D. Corso, S. de Gironcoli, S. Fabris, G. Fratesi, R. Gebauer, U. Gerstmann, C. Gougoussis, A. Kokalj, M. Lazzeri, L. Martin-Samos, N. Marzari, F. Mauri, R. Mazzarello, S. Paolini, A. Pasquarello, L. Paulatto, C. Sbraccia, S. Scandolo, G. Sclauzero, A. P. Seitsonen, A. Smogunov, P. Umari, and R. M. Wentzcovitch, J. Phys. Cond. Matt. **21**, 395502 (2009).
[35] J. P. Perdew and A. Zunger, Phys. Rev. B **23**, 5048 (1981).
[36] D. Vanderbilt, Phys. Rev. B **41**, 7892 (1990).
[37] H. J. Monkhorst and J. D. Pack, Phys. Rev. B **13**, 5188 (1976).
[38] S. Baroni, S. de Gironcoli, A. Dal Corso, and P. Giannozzi, Rev. Mod. Phys. **73**, 515 (2001).
[39] G.-M. Rignanese, X. Gonze, and A. Pasquarello, Phys. Rev. B **63**, 104305 (2001).
[40] G.-M. Rignanese, F. Detraux, X. Gonze, and A. Pasquarello, Phys. Rev. B **64**, 134301 (2001).
[41] X. Zhao and D. Vanderbilt, Phys. Rev. B **65**, 075105 (2002).
[42] C. J. Fennie and K. M. Rabe, Phys. Rev. B **68**, 184111 (2003).
[43] S. M. Nakhmanson, K. M. Rabe, and D. Vanderbilt, Appl. Phys. Lett. **87**, 102906 (2005).
[44] A. R. Akbarzadeh, I. Kornev, C. Malibert, L. Bellaiche, and J. M. Kiat, Phys. Rev. B **72**, 205104 (2005).
[45] A. I. Lebedev, Phys. Solid State **55**, 1198 (2013).
[46] A. I. Lebedev and I. A. Sluchinskaya, Phys. Solid State **55**, 1941 (2013).
[47] Y. Zhang, M. Liu, J. Wang, T. Shimada, and T. Kitamura, J. Appl. Phys. **115**, 224107 (2014).
[48] W. D. Parker and S. M. Nakhmanson, Phys. Rev. B **88**, 035203 (2013).

[49] A. M. Glazer, Acta. Cryst. **B 28**, 3384 (1972).
[50] W. Zhong and D. Vanderbilt, Phys. Rev. Lett. **74**, 2587 (1995).
[51] J. W. Bennett, I. Grinberg, and A. M. Rappe, Phys. Rev. B **73**, 180102 (2006).
[52] A. Bilić and J. D. Gale, Phys. Rev. B **79**, 174107 (2009).
[53] See Supplemental Material at http://link.aps.org/supplemental/10.1103/PhysRevB.91.134103 for JMOL animations of the vibrational modes. The included animations correspond to the distortions of the centrosymmetric $I4/mmm$ RP structure belonging to bands **a** and **c** in Fig. 4 for $\varepsilon_s = -2\%$, -1%, 0.5%, and 0.0%, as well as to bands **g** and **h** for $\varepsilon_s = 3.5\%$. Animations of the AFD distortions for the $Pm\bar{3}m$ $BaZrO_3$ stress-free structure at point R and for the RP structure at points M and A for $\varepsilon_s = 1.5\%$, 2.5%, and 3.5% are also included. JMOL is an open-source Java viewer for chemical structures in 3D. http://www.jmol.org/.
[54] J. Petzelt, Phase Trans. **2**, 155 (1981).
[55] T. Janssen and A. Janner, Adv. Phys. **36**, 519 (1987).
[56] H. Z. Cummins, Phys. Rep. **185**, 211 (1990).
[57] J. D. C. McConnell, Am. Mineral. **68**, 1 (1983).
[58] V. Heine and J. D. C. McConnell, J. Phys. C: Solid State Phys. **17**, 1199 (1984).
[59] G. Łupina, J. Dabrowski, P. Dudek, G. Kozłowski, P. Zaumseil, G. Lippert, O. Fursenko, J. Bauer, C. Baristiran, I. Costina, H.-J. Müssig, L. Oberbeck, and U. Schröder, Appl. Phys. Lett. **94**, 152903 (2009).
[60] We found the values of the spontaneous polarization computed with the linearized approximation of Ref. [43], involving products of $Z^*_{i,\alpha\beta}$ and ionic displacements away from their centrosymmetric positions, to coincide with those obtained using the more accurate Berry-phase method. See, e.g., R. D. King-Smith and D. Vanderbilt, Phys. Rev. B **49**, 5828 (1994) for the description of the latter.
[61] I. Muševič, R. Blinc, and B. Žekš, *The Physics of Ferroelectric and Antiferroelectric Liquid Crystals* (World Scientific, Singapore, 2000).
[62] A. D. Bruce and R. A. Cowley, *Structural phase transitions* (Taylor and Francis, London, 1981).
[63] J. H. Lee, G. Luo, I. C. Tung, S. H. Chang, Z. Luo, M. Malshe, M. Gadre, A. Bhattacharya, S. M. Nakhmanson, J. A. Eastman, H. Hong, J. Jellinek, D. Morgan, D. D. Fong, and J. W. Freeland, Nat. Mater. **13**, 879 (2014).
[64] K. C. Pitike, W. D. Parker, L. Louis, and S. M. Nakhmanson, Phys. Rev. B **91**, 035112 (2015).